Journal of Solar Energy Research (JSER)

Journal homepage: www.jser.ut.ac.ir

A Robust Photovoltaic Power Conditioning System Connected to Weak Grid Through Virtual Impedance Shaping

Majid Hosseinpour[a,*], Rasoul Akbari[a], Mahdi Shahparasti[b]

[a]*Department of Electrical Engineering, University of Mohaghegh Ardabili, Ardabil, Iran*
[b]*School of Technology and Innovations, University of Vaasa, Vaasa, Finland*

ARTICLE INFO

Article Type:

Research Article

Received:2023.12.08
Accepted:2024.07.22

Keywords:
LCL filter
Power Quality
Grid-connected inverter;
Solar array
Impedance shaping

A B S T R A C T

Grid-connected inverters are crucial in transmitting power from distributed production systems and renewable sources to the grid. However, these inverters often generate current harmonics due to high-frequency switching and DC link ripple. To address these issues, various filters, including the LCL filter, are employed. This paper focuses on improving the power quality of grid-connected photovoltaic arrays using LCL filters, primarily through a current sensor and virtual impedance shaping. The paper divides the output impedance of the photovoltaic array power optimization system into an active and passive part. It neutralizes the active component by introducing a series of virtual impedances and counteracts its adverse effects with parallel virtual impedance. The design process for both series and parallel virtual impedance is elaborated, and the system's sensitivity is thoroughly analyzed. To validate the proposed approach, extensive simulations have been carried out using MATLAB software. The simulations demonstrate the robust and precise performance of the control system in effectively injecting the maximum power generated by the photovoltaic array into the grid. Additionally, they showcase the high-quality current being injected into the grid and the system's capacity to maintain stability, even in a weak network environment.

1. Introduction

In recent years, there has been remarkable growth in the adoption of renewable energy sources, driven by concerns over environmental pollution and the diminishing reserves of fossil fuels. Among these renewable sources, photovoltaic (PV) systems have garnered significant attention and popularity, thanks to their distinctive attributes. Power converters transform the generated PV energy and can deliver it to independent loads and the grid. To

*Corresponding Author Email: hoseinpour.majid@uma.ac.ir

Cite this article: Hosseinpour, M., Akbari, R., & Shahparasti, M. (2024). A Robust Photovoltaic Power Conditioning System Connected to Weak Grid Through Virtual Impedance Shaping. Journal of Solar Energy Research, 9(2), 1870-1886. doi: 10.22059/jser.2024.369348.1364

DOI: 10.22059/jser.2024.369348.1364

maximize the power of solar panels, the maximum power point must be considered. Additionally, the power converter systems must be cost-effective, reliable, safe, and have a long lifespan [1].

The distributed energy sources can be connected to the grid via grid-tied inverters. In practical applications, LCL-type grid-tied inverters have been widely utilized due to their superior harmonic mitigation capabilities and compact size. However, these inverters can be sensitive or even vulnerable to network impedance when connected to weak grids, and resonance peaks may occur [2]. Various solutions were proposed for resonance damping, including both passive and active damping methods. Since passive damping involves additional power losses, active damping is preferred [3]. Among active damping methods, current feedback, due to its simplicity and effectiveness, is widely used [4]. Recently, several studies [5] have focused on controlling the injected current into the grid using only one current feedback to reduce the number of sensors. Single-loop grid current control with computational delay and inverter current control with a notch filter are among the proposed methods based on a single current sensor [6]. In single-loop grid current control, grid current feedback with active damping was easily achieved through an optimally designed high-pass filter, providing a wide bandwidth and robustness against LCL parameter variations. Active damping based on a high-pass filter can potentially provide a wider bandwidth and higher robustness compared to active damping methods with computational delay and notch filters [7]. Zhou et al. [8] and Wu et al. [9] introduced and analyzed single-loop grid current control with computational delay based on active damping with a high-pass filter. The delay can impact the performance of active damping. A dual-sampling-based approach for compensating the delay was proposed by Zhou et al. [8]. The design of high-pass filter parameters considering the delay was discussed by Wu et al. [9] and Rasekh et al. [10].

For an LCL-filtered grid-connected inverter, active damping based on network current feedback can ensure the desired bandwidth and good robustness. However, the performance of the inverter is seriously jeopardized by non-ideal conditions at the point of common coupling (PCC), including network voltage distortions and variable network impedance [11]. Active damping based on network current feedback may not work well for wide variations in network impedance. Therefore, the robustness of this control method was discussed, and its relationships with system parameters were extracted and established through mathematical equations [12].

Impedance shaping based on virtual impedance is an effective and enhanced method to control grid-connected inverters in weak and distorted networks [13-15]. An impedance-shaping strategy with parallel and series virtual impedances were proposed by Rasekh et al. [16]. Shaping parallel virtual impedance is equivalent to the voltage feed-forward strategy at the PCC, ensuring system robustness against network disturbances [13, 17]. Impedance shaping through series virtual impedance can be described as canceling the right-half-plane poles in the imaginary axis, thus improving the stability of the system. Essentially, virtual impedance shaping makes the inverter's output impedance passive against network disturbances. Inverters with passive output impedance can ensure system stability regardless of network impedance. A dual-quadrant filter-based approach was used by Akhavan et al. [17] as a parallel compensator with current control to expand the stable operation range and enhance the behavior of a passive grid-connected inverter. According to [18], the optimal active damping gain was proposed for grid-connected inverters with LCL filters to improve passive performance up to the Nyquist frequency range. To improve the passive performance of the grid-connected inverter presented by Wang et al. [19], and to accommodate filter parameter variations, a phase compensator was used in the current controller design by Wang et al. [20]. In the context of enhancing passive performance alongside active damping with capacitor current feedback, reference [21] can be referred to, where a voltage feed-forward technique was employed at the PCC utilizing a low-pass filter. Additionally, the utilization of a proportional controller with a low-pass filter was described by Zhao et al. [22]. Capacitor voltage feedback is also used to improve the passive performance of the grid-connected inverter. For the feedback path transfer function, low-pass filters [18, 23], PI controllers [24], derivative controllers [25], and high-pass filters [26] were employed.

In a majority of the previously discussed methods, the initial step involved the introduction of a specific control approach, after which impedance shaping of the inverter output was examined within the framework of that approach. This approach resulted in a lack of generality. The contributions of this research to address the mentioned limitation are as follows:

- An impedance shaping method that is rooted in a tangible physical concept is introduced for a

photovoltaic array power injection system. A series of virtual impedances have been designed using network current feedback to eliminate the active component.

- In the feedback path, a high-pass filter has been used to avoid undesirable effects of the series virtual impedance at lower frequencies gain and system phase margin.
- Since the use of series virtual impedance may jeopardize the control system's stability around the resonance frequency due to changes in LCL filter parameters, a parallel virtual impedance has been employed using voltage feedback at the PCC to address this issue.
- A systematic and uncomplicated design of control system parameters has been put forth for enhancing the photovoltaic array power injection system. This proposed design has been compared to existing methods in terms of the passive performance of the grid-connected inverter.

Following is an outline of the paper's sections: The second section of the paper outlines the modeling of the photovoltaic array power injection system when connected to the grid through an LCL filter. Following this, the third section introduces a series impedance and a parallel virtual impedance to induce passive behavior, with subsequent parameter tuning and a comparative analysis against existing methods. In the fourth section, sensitivity analysis and comparisons are discussed. The fifth section focuses on the simulation of the studied system, accompanied by an evaluation of its performance. Lastly, the sixth section provides a summary and conclusion.

2. System modeling and passive performance characteristics

2.1. System Overview

Figure 1 depicts the schematic of the photovoltaic array power injection system connected to the grid, incorporating an LCL filter. In this figure, the inductor L1 is on the inverter side, the inductor L2 is on the grid side, and the C signifies the filter capacitor. The network at the PCC is characterized as an ideal voltage source V_g coupled to a network impedance Z_g. The inductance of power lines and transformers, as well as the capacitance of power factor correction circuits, are typically indicative of Z_g [18], which is identified by C_g and L_g. Within the components of the filter and network impedance, there are parasitic resistances that provide a degree of passive damping for system stability. Since considering them complicates the analysis and design of control parameters, in most research, parasitic resistances are ignored in the analysis and control parameter design [23], [27]-[30]. To implement closed-loop control, the network current, denoted as i_g, is measured. The PCC voltage, V_{PCC}, is measured for synchronizing the current with the grid voltage through the phase-locked loop (PLL), where θ represents the tracking angle. The angle θ is combined with the reference current magnitude I^* to form the reference current signal, i_{ref}. Subsequently, the errors are transmitted to the current controller G_c for the generation of modulation signals V_M. Lastly, power-switching gate signals are produced through a pulse width modulation (PWM) modulator.

2.2. Modeling of grid-connected system with LCL filter

As the current loop has a faster dynamic response than the PLL loop, the dissipative properties within the high-frequency region are controlled through the current loop, and within the low-frequency region through both of them. As discussed in [31], the negative effects of the PLL for passive performance may be mitigated by reducing the

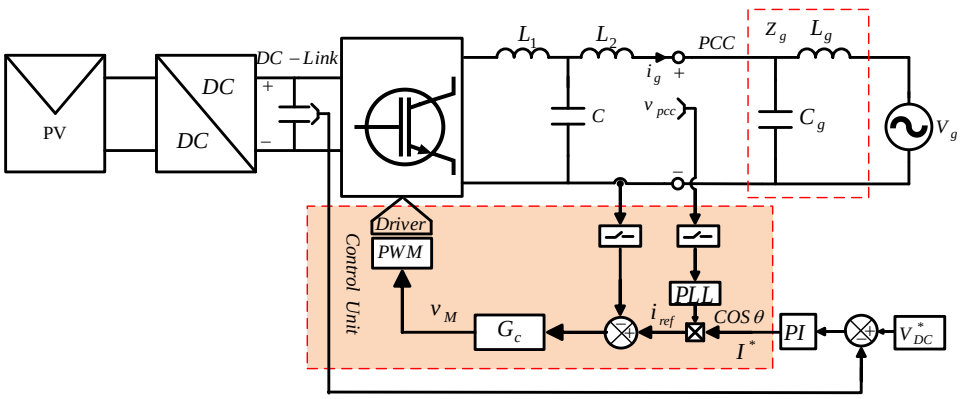

Figure 1. Configuration of grid-connected photovoltaic power optimization system with LCL filter

bandwidth to be lower than the fundamental frequency. Under such conditions, it is possible to omit the PLL in the inverter modeling [29], [32]. Figure 2-a shows the equivalent block diagram of a grid-connected inverter with an LCL filter. According to Equation 1, the current controller G_c employs a proportional resonant (PR) controller [7].

$$G_c(s) = K_p + \frac{2K_r s}{s^2 + \omega_o^2} \quad (1)$$

Coefficients K_p and K_r represent the proportional and resonant gain factors, with ω_o being equivalent to $2\pi f_o$, denoting the fundamental frequency. According to Figure 2-a, G_d symbolizes the temporal lag, equating to the summation of a computational delay relative to the sampling interval (T_s) and a delay associated with a zero-order hold (ZOH), as expounded in Equation 2 [15].

$$G_d(s) = e^{1.5sT_s} \quad (2)$$

Following the equivalent blocks as detailed in reference [33], the block diagram depicted in Figure 2-a is represented in Figure 2-b. Within this figure, G_1 and G_2 expressions can be mathematically expressed using Equations 3 and 4.

$$G_1(s) = \frac{G_d(s)}{s^2 L_1 C + 1} \quad (3)$$

$$G_2(s) = \frac{s^2 L_1 C + 1}{s^3 L_1 L_2 C + s(L_1 + L_2)} \quad (4)$$

Based on the equivalent block diagram in Figure 2-b, the open-loop transfer function T_{ol} or loop gain can be obtained as follows:

$$T_{ol}(s) = G_c(s) G_1(s) G_2(s) \quad (5)$$

The grid current can be expressed as follows:

$$i_g(s) = \frac{T_{ol}(s)}{1+T_{ol}(s)} i_{ref}(s) - \frac{v_{pcc}(s)}{Z_O(s)} \quad (6)$$

where Z_o is the output impedance of the inverter, which is expressed as:

$$Z_o(s) = \frac{1+T_{ol}(s)}{G_2(s)} \quad (7)$$

By substituting 4 and 5 into 7 and updating Z_o, Equation 8 is obtained.

$$Z_o(s) = \frac{sL_2}{1} \times \frac{sL_1}{s^2 L_1 C + 1} + \frac{G_c(s) G_d(s)}{s^2 L_1 C + 1} \quad (8)$$

In the equation above, $Z_{L1C} = sL_1/(s^2L_1C+1)$ represents the impedance resulting from the parallel combination of L_1 and C. Relocating the feedback node i_g within Figure 2-b, shifting it through $G_c'(s)$ input to $G_2'(s)$ input, Figure 3-a is obtained. According to Equation 8, Z_o is broken down into three consecutive elements, including two passive components, $Z_{L2} = sL_2$ and Z_{L1C}, and one active component, $Z_{cl} = G_c(s).G_d(s)/(s^2L_1C+1)$. Therefore, Figure 3-a is reconfigured as Figure 3-b. Physically speaking, the inverter can be represented as an equivalent circuit, as shown in Figure 4, which comprises an ideal current source $[T_{ol}/(1+T_{ol})].i_{ref}$ parallel to the output impedance Z_o.

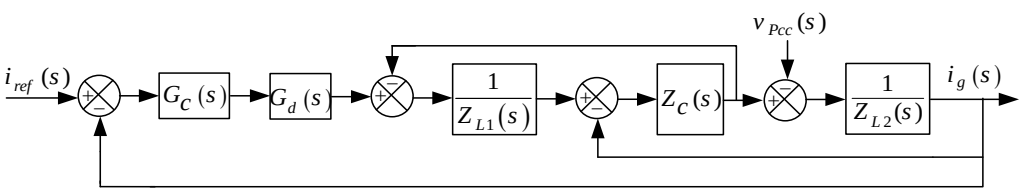

(a)

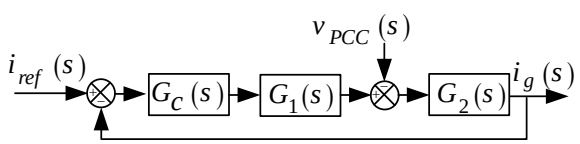

(b)

Figure 2. Block diagram of a grid-tied system using LCL filters, (a) basic block diagram, (b) corresponding block diagram

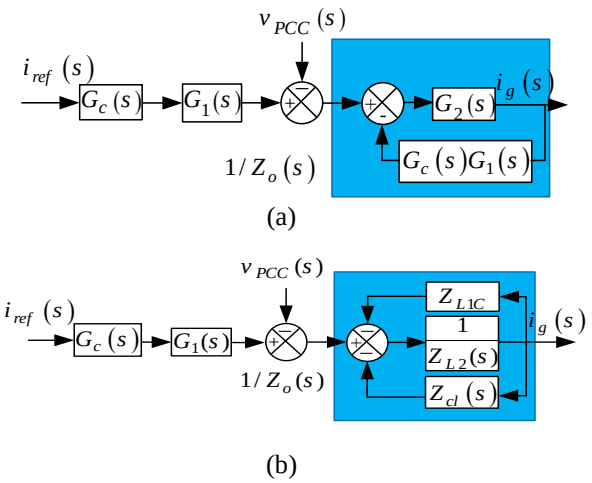

Figure 3. Block diagram for calculation output impedance of the inverter, (a) basic block diagram, (b) corresponding block diagram

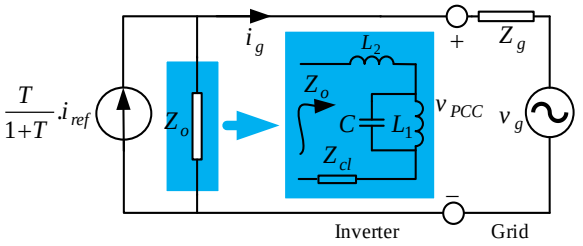

Figure 4. Circuit representation of a grid-tied inverter equipped with an LCL filter

2.3. Passive output impedance performance analysis

Based on Equation 7 and taking into account $v_{PCC} = i_g Z_g + v_g$, Equation 9 can be written.

$$i_g(s) = \left[\frac{T(s)}{1+T(s)} i_{ref(s)} - \frac{v_g(s)}{Z_o(s)}\right] \times \frac{1}{1+Z_g(s)/Z_o(s)} \quad (9)$$

The first part of Equation 9 is not related to the network impedance Z_g and determines the internal stability of the system. achievable through the appropriate design of the parameters of the open-loop transfer function T_{ol}, while ensuring external stability is a more complex task. The second part of Equation 9 can be considered a small and partial loop, with the feedback and forward gains being Z_g/Z_o and unity, accordingly. With this equation, the condition for the external stability of the system is that Z_g/Z_o satisfies the Nyquist stability criteria. More precisely, external stability depends on the phase margin of the impedances Z_g and Z_o (PM_{int}) at their gain crossover frequency (ω_{int}). This phase margin can be expressed by Equation 10.

$$PM_{int} = 180^\circ - [\angle Z_g(j\omega_{int}) - \angle Z_o(j\omega_{int})] \quad (10)$$

To ensure system stability, $PM_{int} > 0$ is expected. Since, in reality, the range of $-90^\circ \le Z_g(j\omega_{int}) \le 90^\circ$ is usually maintained, the network impedance Z_g behaves passively, resulting in external stability with the passive behavior of the output impedance Z_o. Based on Equation 8, there are no real components in both Z_{L2} and Z_{L1C} impedances. Therefore, the real part of the output impedance Z_o corresponds to the impedance Z_{cl}.

As the PR controller is primarily employed to eradicate steady-state tracking errors in the current on the main frequency and exhibits minimal influence on any other frequency, the simplification of the active impedance Z_{cl} in Equation 8 results in Equation 11.

$$Z_{cl}(s) = \frac{K_p G_d(s)}{s^2 L_1 C + 1} \quad (11)$$

Substituting $s=j\omega$ into Equation 11 and considering the part of the impedance Z_{cl}, Equation 12 is obtained, in which $\omega_{L1C} = 1/\sqrt{L_1 C}$

$$\mathrm{Re}[Z_o(j\omega)] = \mathrm{Re}[Z_{cl}(j\omega)] = \frac{K_p \cos(1.5\omega T_s)}{1-(\omega/\omega_{L1C})^2} \quad (12)$$

In Equation 12, the value of K_p is positive, so the passive performance of Z_o hinges on the expressions $1 - (\omega/\omega_{L1C})^2$ and $\cos(1.5\omega T_s)$, that transition from positive to negative values at ω_{L1C} and $\omega_s/6$, respectively. Considering the relationship between ω_{L1C} and $\omega_s/6$, three matching cases can be classified as follows, also shown in Figure 5.

1) If $\omega_{L1C} < \omega_s/6$, $\mathrm{Re}[Z_o(j\omega)] < 0$ results. Therefore, in the frequency range (ω_{L1C}, $\omega_s/6$), the output impedance Zo does not have damping properties.

2) If $\omega_{L1C} > \omega_s/6$, $\mathrm{Re}[Z_o(j\omega)] < 0$ results. Therefore, in the frequency range ($\omega_s/6$, ω_{L1C}), the output impedance Z_o does not have damping properties.

3) If $\omega_{L1C} = \omega_s/6$, $Re[Z_o(j\omega)] \geq 0$ is obtained. Therefore, in the frequency range $(0, \omega_s/6)$, the output impedance Z_o exhibits damping properties.

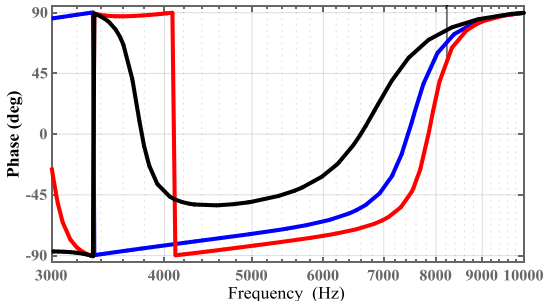

Figure 5. Zo phase diagrams for various values of ωL1C and ωs/6

By examining the three cases above, it is evident that the third case can lead to the passive behavior of the inverter. However, by carefully considering the ωL1C relationship, it can be understood that the passive behavior in the third scenario is susceptible to alterations in the values of L1 and C. Therefore, further improvement of the passive performance is required in the third region as well.

3. Virtual impedance shaping

To bolster the passiveness of the inverter's output impedance, impedance shaping represents a useful strategy. The following part introduces an impedance shaping methodology that relies on both series virtual impedance and parallel virtual impedance.

3.1. Series virtual impedance shaping

As previously mentioned, the range in which the inverter's output impedance Z_o exhibits a passive characteristic is related to the impedance Z_{cl}. As shown in Figure 6, a direct solution for improving the passive performance is to eliminate the impedance Z_{cl} using a series of virtual impedance Z_s. In such conditions, only passive components persist in the inverter's output impedance, ensuring inverter stability.

Based on Figure 3-b, the series virtual impedance Z_s is implemented in the equivalent diagram as shown in Figure 7-a, applying it to the current feedback i_g. To practicable incorporation into the control loop, the i_g feedback node is transferred to the output of the current controller G_c, and the corresponding feedback path is adjusted to $G_s = Z_s/G_1$, as depicted in Figure 7-b. Assuming $Z_s = -Z_{cl}$ and according to Equation 11, the expression for G_s is given by 13.

$$G_s(s) = \frac{Z_s(s)}{G_1(s)} = \frac{-Z_{cl}(s)}{G_1(s)} = -G_c(s) \approx -K_p \qquad (13)$$

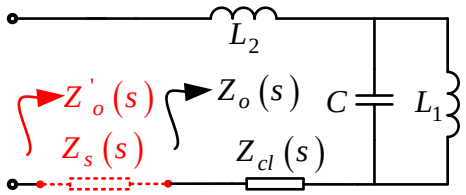

Figure 6. Equivalent circuit of grid-connected inverter output impedance with series virtual impedance

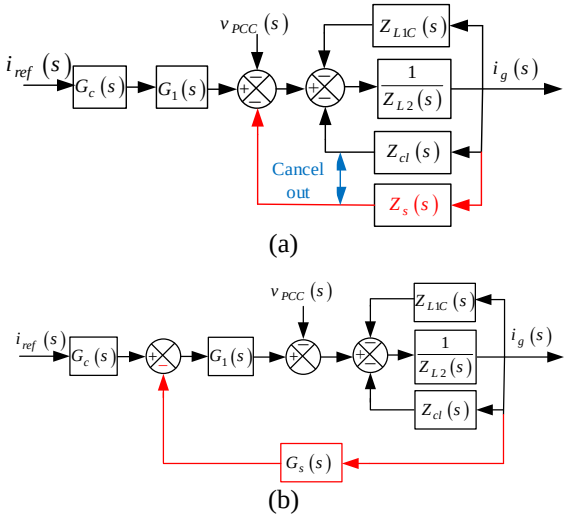

Figure 7. Block diagram for series virtual impedance implementation, (a) basic block diagram, (b) corresponding block diagram

3.2. Practicable challenges of series impedance shaping

By applying the block diagram of Figure 7-b according to Equation 13, the output impedance of the inverter is passively shaped. Since the equivalent value of G_s according to Equation 13 is a negative proportional coefficient, the challenge in this approach is the presence of positive proportional feedback from i_g, which leads to a reduction in the loop gain, particularly at low frequencies. According to Figure 7-b, the loop gain is represented by T' and is expressed based on Equation 14, taking into account the series impedance shaping.

$$T'(s) = \frac{G_c(s)G_d(s)}{s^3 L_1 L_2 C + s(L_1 + L_2) - K_p G_d(s)} \qquad (14)$$

By substituting Equations 1 and 2 into 14 and assuming s = 0, $T'(0)$ = -1 is obtained, indicating a reduction in the loop gain in low-frequency ranges. Furthermore, the coefficient -K_p causes a significant phase drop of T' from 180 degrees, significantly endangering the system's phase margin. To mitigate such detrimental outcomes, the series impedance shaping at low frequencies needs to be inactivated. For this purpose, a high-pass filter G_h is employed, and the modified function G'_s is obtained according to Equation 15, where ω_h represents the high-pass filter's cutoff frequency.

$$G'_s(s) = G_s(s).G_h(s) = -K_p.\frac{s}{s+\omega_h} \tag{15}$$

Using Equation 15, the loop gain in 14 is modified according to Equation 16. Additionally, the modified series virtual impedance, Z'_s, can be expressed as per Equation 17.

$$T''(s) = \frac{G_c(s)G_d(s)}{s^3L_1L_2C + s(L_1+L_2) + G'_s(s)G_d(s)} \tag{16}$$

$$Z'(s) = Z_s(s).\frac{G'_s(s)}{G_s(s)} = -Z_{cl}(s).G_h(s) \tag{17}$$

The modified output impedance of the inverter, Z'_o, is obtained according to Equation 18, and the modified active impedance, Z'_{cl}, is determined as per Equation 19.

$$Z'_o(s) = Z_{L2}(s) + Z_{L1C}(s) + Z'_{cl}(s) \tag{18}$$

$$Z'_{cl}(s) = Z'_s(s) + Z_{cl}(s) = Z_{cl}(s).[1-G_h(s)] \tag{19}$$

Based on Equation 18, it can be deduced that the performance of the passive impedance Z'_o is

contingent on the performance of the active impedance Z'_{cl}. By inserting s = jω in Equation 19, the real component of the modified active impedance Z'_{cl} can be expressed according to Equation 20, in which f(ω) is defined as per Equation 21.

$$\mathrm{Re}[Z'_{cl}(j\omega)] = \frac{K_p\omega_h^2}{\omega^2+\omega_h^2}.\frac{f(\omega)}{1-(\omega/\omega_{L1C})^2} \tag{20}$$

$$f(\omega) = \cos(1.5\omega T_s) - \omega\sin(1.5\omega T_s)/\omega_h \tag{21}$$

By substituting ω = ω_{L1C} into Equation 21 and considering the expression f(ω_{L1C}) = 0, the value of the high-pass filter cutoff frequency can be determined according to Equation 22.

$$\omega_h = \omega_{L1C}\tan(1.5\omega_{L1C}T_s) \tag{22}$$

Figure 8 shows the phase diagram of Z'_o and Z_o. According to this figure, the non-damping part of Z_o, i.e., (ω_s/6, ω_{sg1}), has changed to a part with damping for Z'_o, while Z'_o's damping part, i.e., (ω_s/2, ω_{sg2}), conversely has become non-damping. The new non-damping region of Z_o is due to f(ω) > 0 and 1 - $(\omega/\omega_{L1C})^2$ < 0 within this frequency range. Moreover, the phase diagram of Z'_o remains tangential to the 90-degree and -90-degree lines at ω_{L1C}, meaning that the damping of Z'_o is sensitive to changes in L_1 and C. Therefore, further improvement is needed in the passive performance of the inverter output impedance.

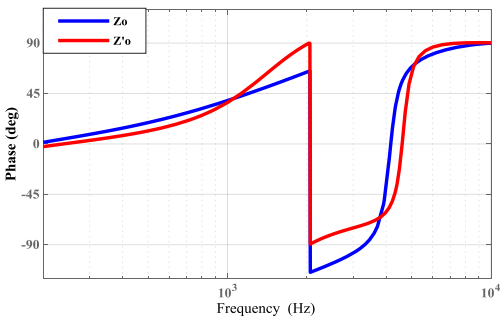

Figure 8. Z_o and Z'_o output impedance phase diagrams

3.3. Parallel impedance shaping

To mitigate the sensitivity of the inverter's output impedance to changes in L_1 and C at the frequency ω_{L1C} when implementing a series impedance shaping, a parallel virtual impedance Z_p, as depicted in Figure 9, has been introduced. The basic schematic diagram for applying Z_p is depicted in Figure 10-a. The transformation of the v_{PCC} input node to the G_c output is presented in the equivalent block diagram, as shown in Figure 10-b, where the expression for G_p is given by Equation 23.

$$G_p(s) = \frac{Z'_o(s)}{Z_p(s)G_1(s)} \tag{23}$$

According to Equation 23, the parallel virtual impedance Z_p is implemented through feedback from v_{PCC} using the transfer function G_p. Thus, the inverter output impedance is even more shaped, resulting in Equation 24, which can be expressed as Equation 25 by substituting s = jω.

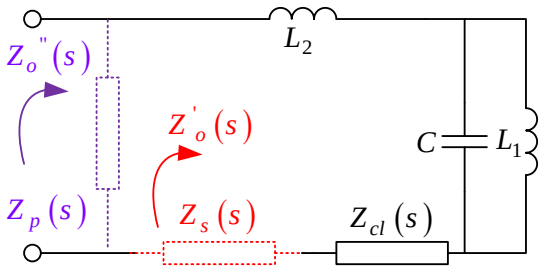

Figure 9. Equivalent circuit of inverter output impedance containing virtual parallel and series impedances

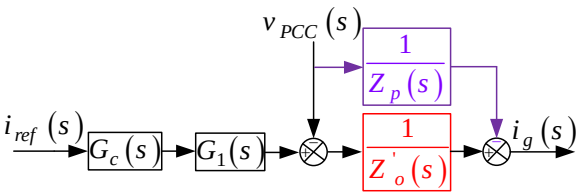

(a)

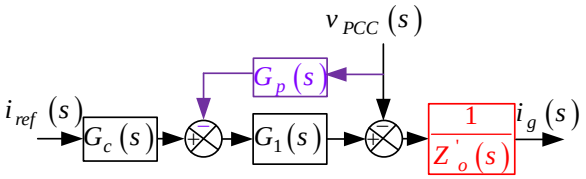

(b)

Figure 10. Block diagram for parallel virtual impedance implementation, (a) basic block diagram, (b) corresponding block diagram

$$Z_o''(s)=\frac{Z_o'(s)Z_p(s)}{Z_o'(s)Z_p(s)}=\frac{1}{1+G_p(s)G_1(s)}.Z_o' \quad (24)$$

$$Z_o''(j\omega)=\frac{1}{1+G_p(j\omega)G_1(j\omega)}Z_o'(j\omega) \quad (25)$$

The phase relationship corresponding to Equation 25 can be expressed by Equation 26.

$$\angle Z''_o(j\omega) - \angle Z'_o(j\omega) = -\angle[1 + G_p(j\omega)G_1(j\omega)] \quad (26)$$

To determine an appropriate G_p, the phase margin of the expression $1 + G_p(j\omega)G_1(j\omega)$ needs to be specified. According to Equation 26, the phase margin of this expression corresponds to the disparity between $\angle Z'_o$ and $\angle Z''_o$. The value of $\angle Z'_o$ is obtained based on Figure 9. Assuming that Z''_o is passively shaped, its phase angle will be in the range of $-90° < Z''_o(j\omega) < 90°$, and the resulting phase margin of the expression $1 + G_p(j\omega)G_1(j\omega)$ is calculated as per Table 1.

Table 1. Expected phase of expression $1 + G_p(j\omega)G_1(j\omega)$

$\omega < \omega_{L1C}$	$\omega > \omega_{L1C}$	
	$\omega_{L1C} < \omega \le \omega_{sg2}$	$\omega_{sg2} < \omega \le \omega_s / 2$
Leading phase	Lagging phase	Leading phase

When the phase of $G_1(j\omega)$ is accurately defined, it leads to the derivation of an expression for G_p that aligns with the criteria outlined in Table 1. Typically, it is configured to guarantee a satisfactory reduction in switching frequency, where $\omega_{L1C} < \omega_s/3$ [34, 35]. Taking into account Equation (3) and the relationship expressed as $\angle G_1(j\omega) = -1.5\omega T_s$, G_p is described as a negative proportional gain denoted as $G_p(s) = -K_{pf}$. This approach establishes a positive proportional feedback loop from v_{PCC} to shape the parallel impedance. Thus, the complete control block diagram of the grid-connected inverter, including shaping the virtual series and parallel impedance, is shown in Figure 11.

3.4. Virtual impedance shaping parameter setting

The following procedures are explained step by step to set the virtual impedance shaping parameters.

Step 1: Compute the cutoff frequency (ω_h) for the high-pass filter using Equation 22.

Step 2: Using the adapted loop gain T″ as per Equation 16, ascertain the criteria for the crossover frequency (f_c), gain margin (GM), and phase margin(PM).

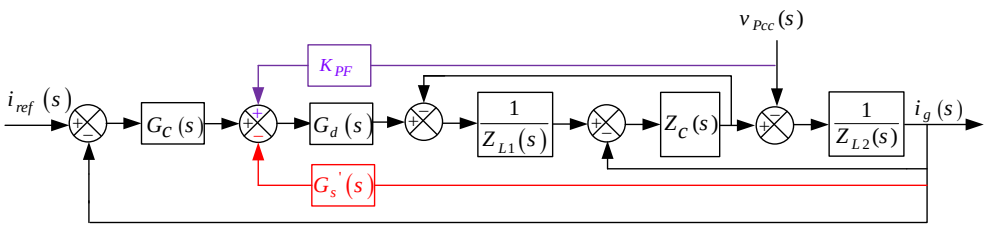

Figure 11. Detailed virtual series block diagram and parallel impedance shaping method

Table 2. The values of the under-consideration system parameters

Parameter	Value	Parameter	Value
Sampling frequency	20 kHz	Output power	5 kW
Inverter side inductor	600 µH	Input voltage	365 V
Grid side inductor	150 µH	Grid voltage (RMS)	220 V
Filter capacitor	10 µF	Switching frequency	10 kHz

Step 3: Adjust the current controller parameters, including the coefficients K_p and K_r, to ensure inverter stability based on modified loop gain T.

Step 4: Generate the phase diagram for Z''_o utilizing Equation 24 by appropriately increasing the K_{pf} coefficient.

Step 5: Choose a suitable value for K_{pf} and investigate the passive characteristics of the inverter's output impedance.

To evaluate the effectiveness of the parameter tuning process, the control coefficients are determined using the initial sample values as provided in Table 2. While designing the LCL filter, several common constraints are considered. These constraints include ensuring that the current ripple on the inverter side remains below 30% of the nominal main current, the reactive power of the filter capacitor stays below 5% of the nominal output power, and the switching harmonic remains under 0.3% of the nominal current.

In the first step, the high-pass filter cutoff frequency, ω_h, is calculated to be approximately 1880 rad/sec using Equation 22. Then, the current controller values, K_r and K_p, are adjusted based on the specifications of the crossover frequency, f_c, gain margin, GM, and phase margin, PM. To achieve an appropriate dynamic response, the crossover frequency is typically set to be 10% of the switching frequency. An ideal phase margin, PM, typically falls within the range of 30 to 60 degrees. A recommended gain margin, GM, is typically less than 2 dB. Considering these requirements, K_p is set to 3.8 Ω, and K_r is set to 290 Ω/s. According to Figure 12, the modified loop gain, T'', based on Equation 16, is obtained with f_c = 1 kHz, PM = 45°, GM_1 = 8.7 dB, and GM_2 = -9.8 dB. These values indicate acceptable stability for the inverter. Finally, with the help of plotting the Bode diagrams for various values of K_{pf}, this coefficient is also adjusted. Phase diagrams of Z''_o for increasing K_{pf} from zero to 0.51 are shown in Figure 13. According to this figure, the K_{pf} coefficient increases the inverter output impedance's damping behavior at high frequencies, while it reduces at low frequencies. By selecting K_{pf} in the range (0.1, 1), the phase diagram of Z''_o remains in a range of ±90 degrees. This means that the output impedance of the inverter exhibits damping behavior up to the Nyquist frequency. However, choosing a low value of K_{pf} can result in suboptimal dynamic behavior in the presence of voltage disturbances. Based on the variations in LCL filter parameters, K_{pf} should not be close to the boundary values of 0.10 or 1. Therefore, with these considerations, K_{pf} = 0.6 is chosen.

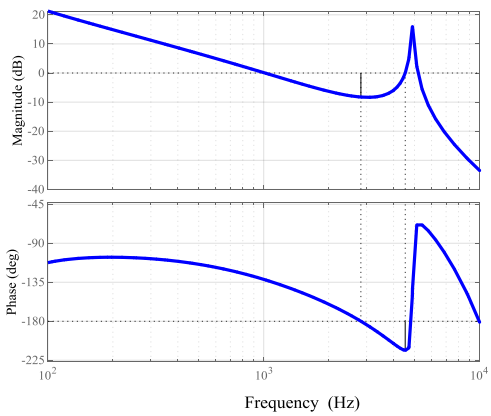

Figure 12. The Bode diagram of loop gain T" based on equation 16

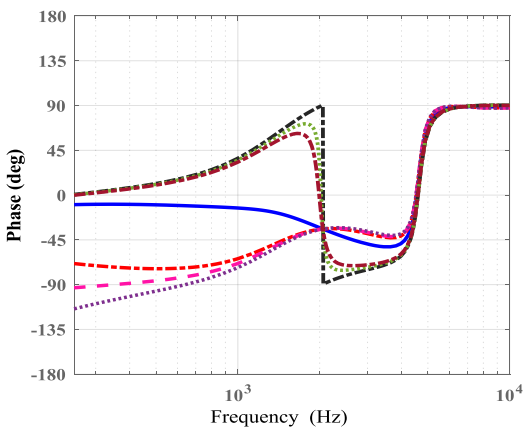

Figure 13. Z''_o phase diagram with different K_{pf} values

3.5. Sensitivity analysis

The sensitivity of the proposed method to variations in the inductance and capacitance values of the LCL filter is considered in this section. The deviations in these parameters may occur over time or due to various other reasons and depend on operational conditions and manufacturing errors. Typically, changes of 20% for inductance and 10% for capacitance are taken into account [16]. Based on this, two scenarios involving a 20% increase and a 20% decrease in the values of the inductors (L_1 and L_2) and a 10% change in the value of the capacitor (C) were selected. The phase diagrams associated with Z''_o in Figure 14 illustrate that, even after implementing these changes, the phase diagrams remain within the range of (-90°, 90°). This indicates that the damping property of the shaped output impedance is maintained up to the Nyquist frequency, highlighting the robustness of the proposed approach in the face of variations in the LCL filter parameters.

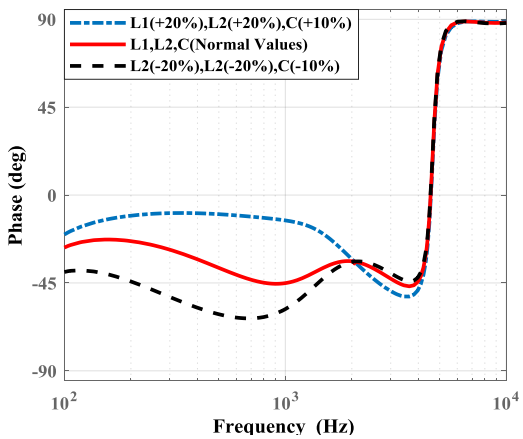

Figure 14. Z''_o phase diagram in sensitivity analysis

3.6. Comparison with similar methods

The proposed approach for shaping impedance in grid-tied photovoltaic arrays has been examined with established techniques, that are discussed below.

A. Additional Sensors: In [18], [21], [23], the need for an extra current or voltage sensor is stipulated to measure the capacitor voltage and current. In contrast, the proposed method and methods outlined in [27] and [36] do not require such sensors.

B. Passive performance: In [27], the damping property of the inverter's output impedance is not attained at high frequencies, while similar approaches can accomplish this up to the frequency $\omega_s/2$.

C. Robustness: In [27], robustness against variations in filter parameters around the frequency ω_{L1C} is weak, whereas other methods perform better in this regard.

D. Complexity: In [27], the associated design procedure relies on a single-loop control, in which numerical computations, including pole-zero and Bode plots, are used. In [18], [23], the design process is grounded in a multi-loop control, exclusively employing analytical equations. Contrary to this, the proposed method's design process employs a multi-loop control approach that combines both analytical equations and numerical computations. Generally, such techniques tend to be relatively uncomplicated as they utilize single-loop control or analytical equations. The design process in [21] is likewise rooted in a multi-loop control. However, it exclusively uses numerical computations, exhibiting a moderate degree of complexity. The same scenario is evident in [22], although an extra sensor is used in that case.

Compared to previous approaches, the proposed approach not only achieves effective damping up to the frequency $\omega_s/2$, but also exhibits considerable stability in the face of variations in LCL filter parameters, and has a simple control structure. Cost-wise, the control system is also affordable.

4. Simulation results

The power conditioning system of the photovoltaic array has been simulated and evaluated for a 5 kW output power. The output voltage of the photovoltaic array is boosted using a boost converter, and maximum power point tracking (MPPT) is applied. The energy produced by the system is then injected into the grid using an inverter connected to an LCL filter. The power conditioning system of the photovoltaic array is analyzed with and without the presence of virtual impedances, both series and parallel. To demonstrate the dynamic behavior of the photovoltaic power conditioning system, variations in temperature and solar irradiance on the photovoltaic array are considered to assess the tracking speed and accuracy of the reference current. The system parameters are provided in Table 2. The PI controller coefficients and the DC link voltage between the DC-DC converter and the grid-connected inverter are selected as K_P=0.9, K_I=22, and 360 volts, respectively. Additionally, the solar system parameters are presented in Table 3.

Table 3. Solar panel parameters at 25˚C and 1000W/m^2 radiation intensity.

Parameter	Value
I_{mp}	5.45 A
V_{mp}	54.2 V
P_{max}	295.39 W
I_{sc}	5.83 A
V_{oc}	63.3 V
N_s	3
N_p	6

Figure 15 shows the PCC voltage and the injected current of the photovoltaic power conditioning system into the grid. According to this figure, the injected current is in phase with the PCC voltage. It should be noted that the injected current into the grid has been multiplied by five for better visualization. In Figure 16, the Total Harmonic Distortion (THD) of the injected current into the grid is presented. According to this figure, the quality of the injected current into the grid is quite good, with a THD of 1.75%. Furthermore, the predominant part of this distortion is due to the third harmonic distortion, which is caused by minor fluctuations in the DC link voltage of the inverter. These voltage fluctuations in the DC link are inevitable and result from the photovoltaic array operation and MPPT by the DC-DC converter. Precision in the frequency spectrum indicates that apart from a 1.25% distortion in the third harmonic, the performance of the power conditioner system is adequate, and no other significant harmonics are observed in the frequency spectrum.

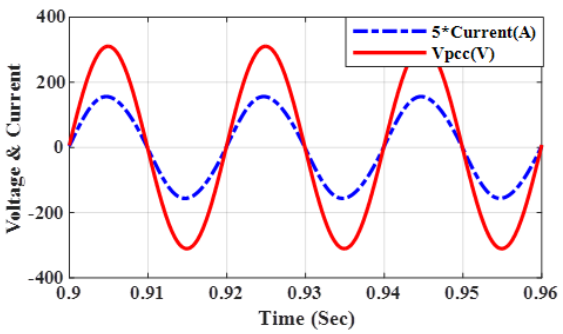

Figure 15. Output voltage and current of the grid-connected photovoltaic array in the presence of virtual impedances

Figure 17 shows the network's current and voltage in the presence and absence of virtual impedances. According to this figure, from the beginning until 0.35 seconds, the photovoltaic power conditioning system operates with the presence of series and parallel virtual impedances. At 0.35 seconds, the series and parallel virtual impedances are removed from the control system, and subsequently, the output voltage and current experience severe ripples, practically necessitating the system to be disconnected from the power grid.

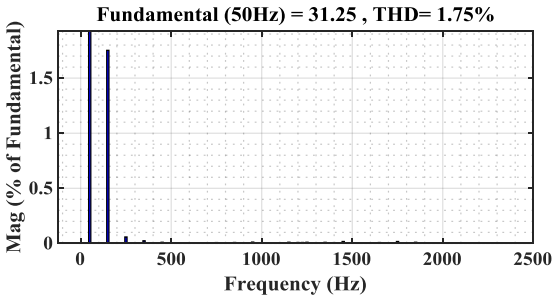

Figure 16. THD of injected current to the grid

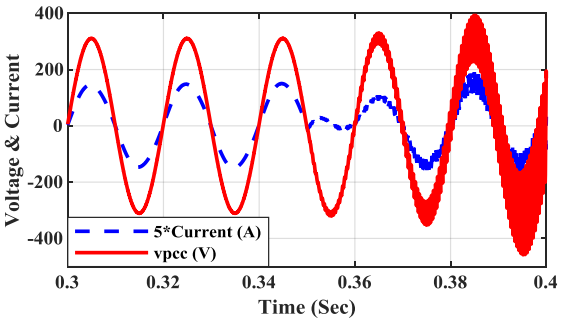

Figure 17. Grid voltage and current with and without the presence of virtual impedances

In Figure 18, a power-voltage and a current-voltage curve of the photovoltaic array are depicted. As indicated in this figure, the power optimization system for the studied photovoltaic array is capable of generating a maximum power output of approximately 5 kW under conditions of 1000 W/m^2 irradiance and a temperature of 25˚C. The MPPT system aims to maximize the obtainable power from the photovoltaic array at each point.

To assess the dynamic performance of the power optimization system for varying inputs of the photovoltaic array, the solar irradiance decreased from 1000 W/m^2 to 700 W/m^2 within the time interval [0.5, 0.8]. The response of the system, the way the photovoltaic array generates current and power, as well as the injected power and current into the grid, have been examined.

Figure 19 depicts the output current of the photovoltaic array. According to this figure, as the irradiance intensity decreases, the generated current by the photovoltaic array drops from 28 A to 19 A

and stabilizes after approximately 0.1 seconds. Conversely, when the irradiance intensity increases, the array's current recovers to a new stable condition, reaching 28 A in approximately 0.15 seconds. In Figure 20, the generated power of the photovoltaic array is illustrated. At an irradiance of 1000 W/m² and a temperature of 25˚C, the system produces approximately 9.4 kW of power. As irradiance intensity decreases, the power output drops to approximately 3.5 kW, but it promptly and

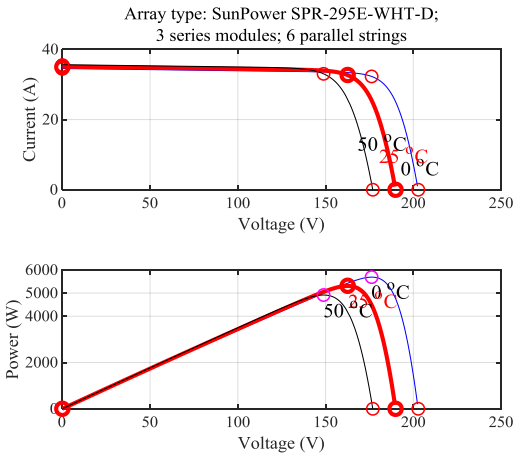

Figure 18. Characteristic curves of the photovoltaic array used in the study, a) I-V curve, b) P-V curve

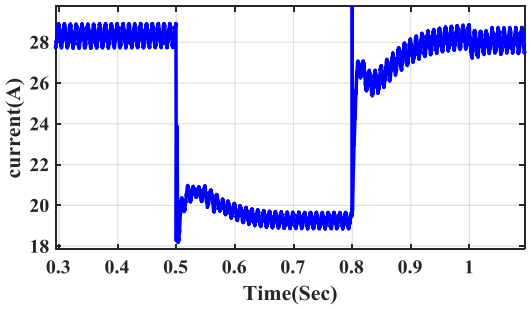

Figure 19. Photovoltaic array output current

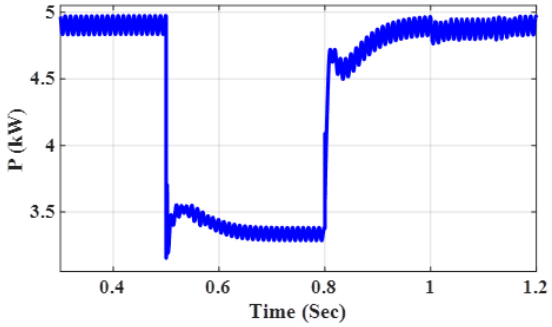

Figure 20. Photovoltaic array output power

effectively rebounds to its previous level as irradiance intensity increases once more.

The voltage of the DC link capacitor, situated between the DC-DC converter and the grid-connected inverter, plays a balancing role in power injection into the grid. By controlling the voltage of this capacitor, the power generated by the photovoltaic array can be controlled and transferred to the grid. At 0.5 seconds, as the irradiance intensity decreases, the output power of the photovoltaic array decreases, which is indicated by the reduction in the voltage of the DC link capacitor. The PI controller of the DC link responds to this by reducing the reference current of the inverter and strives to maintain the voltage of the DC link capacitor at its reference level. This is achieved within approximately 0.5 seconds, stabilizing the voltage of the DC link capacitor. As a result, the injected current to the grid decreases under these conditions, aligning itself with the reduced current and power of the photovoltaic array. Following the increase in solar radiation intensity at 0.8 seconds, the injected power from the photovoltaic array to the DC link capacitor increases, and the DC link voltage increases momentarily. This time, the DC link PI controller increases the reference current of the inverter to transfer the stored excess energy in the capacitor to the grid and stabilize the DC link voltage at the previous reference level. After about 0.15 seconds, the DC link capacitor voltage and the injected current to the grid reach stable conditions. In Figure 21, the DC link capacitor voltage is displayed. According to this figure, the DC link voltage oscillates slightly around 360 V, with fluctuations of about 4 V, and the DC link voltage control system operates satisfactorily. Figure 22 depicts the inverter output current, and in Figure 23, the injected power from the power conditioning system to the grid during a period of fluctuating solar radiation intensity is displayed. According to these two figures, the current and injected power to the grid decrease and increase in line with changes in radiation intensity and reach new stable conditions within a short time, indicating the suitable dynamic performance of the proposed control system.

Table (4) shows a comparison between the proposed method and recent research in the field of the performance improvement of the grid-connected inverter. In this Table, the compared references have been evaluated in terms of the control strategy, considering the delay effect on the control process, the number of current and voltage sensors, and the THD value of the injected current to

Table 4. Comparison of proposed method and recent similar research

	Ref. [37]	Ref. [38]	Ref. [39]	Ref. [40]	Ref. [41]	Ref. [42]	Proposed Method
Control Strategy	Capacitor Voltage Feedback	LMI-LQR Current Control	Jaya based MPPT	Inverter Side Current Feedback	Quasi-Predictive Control	Virtual Impedance & Capacitor Current Feedback	Grid Side Current Feedback
Delay effect	✓	✓	×	×	✓	✓	✓
Sensors Count	2	3	3	2	3	3	2
Grid current THD (Reported)	3.47%	2.43%	2.8%	4.82%	2.15%	1.76%	1.75%

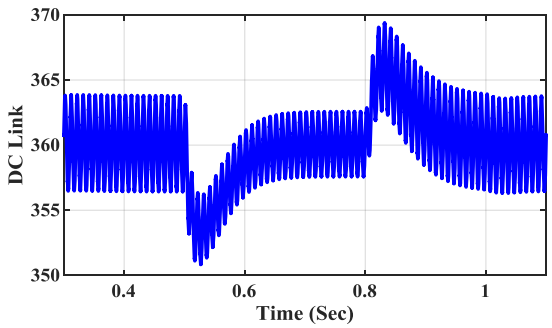

Figure 21. DC link voltage

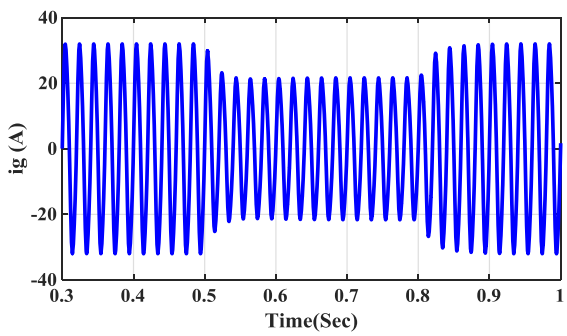

Figure 22. Grid current for different radiation

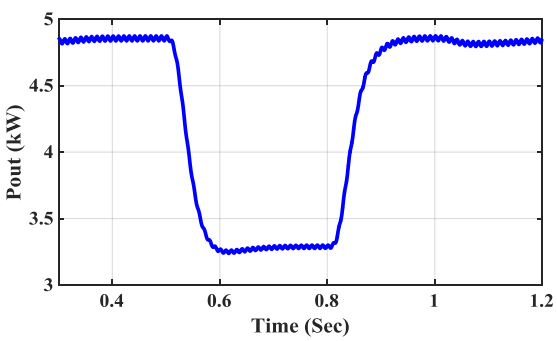

Figure 23. Injection of photovoltaic array power to the grid for different radiations

the network. According to this Table, some of the mentioned cases have been included in the comparative references and some have not been evaluated. In the proposed method, the delay effect on the control loops is considered and the number of required sensors is less or equal to other similar methods. In addition, the grid-injected current THD under the conditions of the related reference is also presented in Table (4). Regarding the validation and comparison with other research and according to the IEEE-1547 standard, the quality of the grid injected current in the low voltage network should be such that the current THD would be less than 5% while the amount of each harmonic order would be less than 3%. Because the quality of the grid injected current is 1.73%, the modeling and control presented in this research have sufficient accuracy. It is worth mentioning that presenting the THD value is just to complete the information provided and the comparison of THD values with each other cannot be cited due to the difference in the conditions considered in each reference.

The main characteristic of the weak network is the change in the impedance range of the network, and the performance of the control system in such conditions is investigated in this article. One of the common problems in a weak network is the low voltage quality at the point of common coupling, which can affect the performance of the grid-connected inverter. The future work in the field of this research can be a performance investigation of an improved control structure for the system under study in a distorted and harmonically polluted network. In such a situation, a modified control scheme should be designed, if needed, for high-quality current injection in the harmonics-polluted network.

5. Conclusion

In this study, an approach for the enhancement of grid-connected photovoltaic array power conditioning systems is presented. The utilization of

an LCL filter and a tailored control method is employed to improve the quality of injected current. In parallel, stability and passive system performance are ensured through the application of an advanced virtual impedance shaping technique. The inverter output impedance is partitioned into two essential components, one passive and the other active, connected in series. To nullify the active component, a virtual series impedance is employed, guided by grid current feedback. To mitigate any potential adverse influences on the system's low-frequency loop gain and phase margin, a high-pass filter modification is incorporated into the feedback function. Simultaneously, a parallel virtual impedance is introduced through PCC voltage feedback, augmenting system stability and passive performance. The proposed control methodology has been applied to the photovoltaic array's power conditioning system, linked to the grid. Comprehensive evaluations have been carried out under stable conditions and simulated disturbances arising from fluctuations in solar irradiance. The simulation results consistently affirm the high quality of the injected current into the grid. Notably, the system retains its stability and passive performance, even when confronted with substantial variations in the network impedance. These results underscore the effectiveness and resilience of the approach in optimizing photovoltaic power conditioning system performance in grid-connected scenarios.

Nomenclature:

AD	Active damping
V_g	Grid's voltage
PCC	Point of common coupling
f_o	Fundamental frequency
f_c	Crossover frequency
i_{L2}	Injected current to the grid
PLL	Phase-locked loop
$G_c(s)$	Current regulator
G_d	Dealy transfer function
i_c	Capacitor current
T_s	Sampling period
K_p	Proportional gain
K_r	Resonant gain
L_1	Inverter side inductor of LCL filter
L_2	Grid side inductor of LCL filter
C	Capacitor of LCL filter
T_{ol}	Loop gain of current control loop
ω_0	Fundamental angular frequency
ω_i	resonance bandwidth
ω_r	LCL angular resonance frequency
ω_h	High-pass filter cutoff frequency
PM	Phase margin
GM	Gain margin
Z_g	Network impedance
Z_o	Output impedance of the inverter
AD	Active damping
V_g	Grid's voltage
PCC	Point of common coupling
i_{L2}	Injected current to the grid
PLL	Phase-locked loop
$G_c(s)$	Current regulator
i_C	Capacitor current
T_s	Sampling period
K_p	Proportional gain
K_r	Resonant gain
ω_0	Fundamental angular frequency
ω_i	resonance bandwidth
ω_r	LCL angular resonance frequency

References:

[1] Hosseinpour, M., Dastgiri, A. and Shahparasti, M., 2024. Design and Analysis of a Power Quality Improvement System for Photovoltaic Generation Based on LCL-Type Grid Connected Inverter. *International Journal of Engineering*, *37*(2), pp.252-267. https://doi.org/10.5829/ije.2024.37.02b.04

[2] He, Y., Wang, X., Ruan, X., Pan, D. and Qin, K., 2020. Hybrid active damping combining capacitor current feedback and point of common coupling voltage feedforward for LCL-type grid-connected inverter. *IEEE Transactions on Power Electronics*, *36*(2), pp.2373-2383. https://doi.org/10.1109/TPEL.2020.3008160

[3] He, Y., Wang, X., Pan, D., Ruan, X. and Su, G., 2021. An ignored culprit of harmonic oscillation in LCL-type grid-connected inverter: Resonant pole cancelation. *IEEE Transactions on Power Electronics*, *36*(12), pp.14282-14294. https://doi.org/10.1109/TPEL.2021.3084810

[4] Zhang, H., Ruan, X., Lin, Z., Wu, L., Ding, Y. and Guo, Y., 2021. Capacitor voltage full feedback scheme for LCL-type grid-connected inverter to suppress current distortion due to grid voltage harmonics. *IEEE Transactions on Power*

Electronics, *36*(3), pp.2996-3006. https://doi.org/10.1109/TPEL.2020.3014338
[5] Zou, C., Liu, B., Duan, S. and Li, R., 2014. Influence of delay on system stability and delay optimization of grid-connected inverters with LCL filter. *IEEE Transactions on Industrial Informatics*, *10*(3), pp.1775-1784. https://doi.org/10.1109/TII.2014.2324492
[6] Yao, W., Yang, Y., Zhang, X., Blaabjerg, F. and Loh, P.C., 2017. Design and analysis of robust active damping for LCL filters using digital notch filters. *IEEE Transactions on Power Electronics*, *32*(3), pp.2360-2375. https://doi.org/10.1109/TPEL.2016.2565598
[7] Rasekh, N. and Hosseinpour, M., 2020. Adequate tuning of LCL filter for robust performance of converter side current feedback control of grid connected modified–Y-source inverter. *International Journal of Industrial Electronics Control and Optimization*, *3*(3), pp.365-378. https://doi.org/10.22111/ieco.2020.32122.1221
[8] Zhou, L., Chen, Y., Luo, A., Guerrero, J.M., Zhou, X., Chen, Z. and Wu, W., 2016. Robust two degrees- of- freedom single- current control strategy for LCL- type grid- connected DG system under grid- frequency fluctuation and grid- impedance variation. *IET Power Electronics*, *9*(14), pp.2682-2691. https://doi.org/10.1049/iet-pel.2016.0120
[9] Wu, W., Peng, L., Qi, Y., Liu, Q., Huang, Z., Dong, F., Chen, M. and Wang, B., 2017, October. An improved active damping method with grid-side current feedback to maximize damping ratio for LCL-type grid-connected inverter. In *2017 IEEE Energy Conversion Congress and Exposition (ECCE)* (pp. 5607-5611). IEEE. https://doi.org/10.1109/ECCE.2017.8096933
[10] Rasekh, N., Rahimian, M.M., Hosseinpour, M., Dejamkhooy, A. and Akbarimajd, A., 2019, February. A step by step design procedure of PR controller and capacitor current feedback active damping for a LCL-type grid-tied T-type inverter. In *2019 10th International Power Electronics, Drive Systems and Technologies Conference (PEDSTC)* (pp. 612-617). https://doi.org/10.1109/PEDSTC.2019.8697853
[11] Zhu, K., Sun, P., Zhou, L., Du, X. and Luo, Q., 2020. Frequency-division virtual impedance shaping control method for grid-connected inverters in a weak and distorted grid. *IEEE Transactions on Power Electronics*, *35*(8), pp.8116-8129. https://doi.org/10.1109/TPEL.2019.2963345
[12] Xu, J., Xie, S., Zhang, B. and Qian, Q., 2018. Robust grid current control with impedance-phase shaping for LCL-filtered inverters in weak and distorted grid. *IEEE Transactions on Power Electronics*, *33*(12), pp.10240-10250. https://doi.org/10.1109/TPEL.2018.2808604
[13] Chen, X., Zhang, Y., Wang, S., Chen, J. and Gong, C., 2017. Impedance-phased dynamic control method for grid-connected inverters in a weak grid. *IEEE Transactions on Power Electronics*, *32*(1), pp.274-283. https://doi.org/10.1109/TPEL.2016.2533563
[14] Hosseinpour, M., Asad, M. and Rasekh, N., 2021. A step-by-step design procedure of a robust control design for grid-connected inverter by LCL filter in a weak and harmonically distorted grid. *Iranian Journal of Science and Technology, Transactions of Electrical Engineering*, *45*, pp.843-859. https://doi.org/10.1007/s40998-021-00414-z
[15] Hosseinpour, M., Sabetfar, T. and Shahparasti, M., 2023. Grid- tied PEMFC power conditioning system based on capacitor voltage thorough feedback procedure in a weak and harmonics- polluted network. *Energy Science & Engineering*. https://doi.org/10.1002/ese3.1624
[16] Rasekh, N. and Hosseinpour, M., 2020. LCL filter design and robust converter side current feedback control for grid-connected Proton Exchange Membrane Fuel Cell system. *International Journal of Hydrogen Energy*, *45*(23), pp.13055-13067. https://doi.org/10.1016/j.ijhydene.2020.02.227
[17] Akhavan, A., Vasquez, J.C. and Guerrero, J.M., 2020. A simple method for passivity enhancement of current controlled grid-connected inverters. *IEEE Transactions on Power Electronics*, *35*(8), pp.7735-7741. https://doi.org/10.1109/TPEL.2020.2967239
[18] Xie, C., Li, K., Zou, J. and Guerrero, J.M., 2019. Passivity-based stabilization of LCL-type grid-connected inverters via a general admittance model. *IEEE Transactions on Power Electronics*, *35*(6), pp.6636-6648. https://doi.org/10.1109/TPEL.2019.2955861
[19] Wang, X., He, Y., Pan, D., Zhang, H., Ma, Y. and Ruan, X., 2022. Passivity enhancement for LCL-filtered inverter with grid current control and capacitor current active damping. *IEEE Transactions on Power Electronics*, *37*(4), pp.3801-3812. https://doi.org/10.1109/TPEL.2021.3111677
[20] Wang, C., Wang, X., He, Y., Pan, D., Zhang, H., Ruan, X. and Chen, X., 2023. Passivity-Oriented Impedance Shaping for LCL-Filtered Grid-Connected Inverters. *IEEE Transactions on Industrial Electronics*, *70*(9), pp.9078-9090. https://doi.org/10.1109/TIE.2022.3210573

[21] Akhavan, A., Mohammadi, H.R., Vasquez, J.C. and Guerrero, J.M., 2020. Passivity-based design of plug-and-play current-controlled grid-connected inverters. *IEEE Transactions on Power Electronics*, *35*(2), pp.2135-2150. https://doi.org/10.1109/TPEL.2019.2920843

[22] Zhao, J., Xie, C., Li, K., Zou, J. and Guerrero, J.M., 2022. Passivity-oriented design of LCL-type grid-connected inverters with Luenberger observer-based active damping. *IEEE Transactions on Power Electronics*, *37*(3), pp.2625-2635. https://doi.org/10.1109/TPEL.2021.3109434

[23] Xie, C., Li, K., Zou, J., Liu, D. and Guerrero, J.M., 2020. Passivity-based design of grid-side current-controlled LCL-type grid-connected inverters. *IEEE Transactions on Power Electronics*, *35*(9), pp.9813-9823. https://doi.org/10.1109/TPEL.2020.2971380

[24] Yang, Z., Shah, C., Chen, T., Teichrib, J. and De Doncker, R.W., 2021. Virtual damping control design of three-phase grid-tied PV inverters for passivity enhancement. *IEEE Transactions on Power Electronics*, *36*(6), pp.6251-6264. https://doi.org/10.1109/TPEL.2020.3035417

[25] Rodriguez-Diaz, E., Freijedo, F.D., Guerrero, J.M., Marrero-Sosa, J.A. and Dujic, D., 2019. Input-admittance passivity compliance for grid-connected converters with an LCL filter. *IEEE Transactions on Industrial Electronics*, *66*(2), pp.1089-1097. https://doi.org/10.1109/TIE.2018.2835374

[26] Hans, F., Schumacher, W., Chou, S.F. and Wang, X., 2019. Passivation of current-controlled grid-connected VSCs using passivity indices. *IEEE Transactions on Industrial Electronics*, *66*(11), pp.8971-8980. https://doi.org/10.1109/TIE.2018.2883261

[27] Rasekh, N., Hosseinpour, M., Dejamkhooy, A. and Akbarimajd, A., 2021. Robust power conditioning system based on LCL-type quasi-Y-source inverter for grid connection of photovoltaic arrays. *International Journal of Automation and Control*, *15*(6), pp.692-709. https://doi.org/10.1504/IJAAC.2021.118526

[28] Harnefors, L., Bongiorno, M. and Lundberg, S., 2007. Input-admittance calculation and shaping for controlled voltage-source converters. *IEEE transactions on industrial electronics*, *54*(6), pp.3323-3334. https://doi.org/10.1109/TIE.2007.904022

[29] Hosseinpour, M., Sabetfar, T., Dejamkhooy, A. and Shahparasti, M., 2023. Design and control of LCL-type grid-tied PV power conditioning system based on inverter and grid side currents double feedback. *International Journal of Modelling and Simulation*, pp.1-21. https://doi.org/10.1080/02286203.2023.2204319

[30] Wu, H. and Wang, X., 2020. Virtual-flux-based passivation of current control for grid-connected VSCs. *IEEE Transactions on Power Electronics*, *35*(12), pp.12673-12677. https://doi.org/10.1109/TPEL.2020.2997876

[31] Harnefors, L., Wang, X., Yepes, A.G. and Blaabjerg, F., 2016. Passivity-based stability assessment of grid-connected VSCs—An overview. *IEEE Journal of emerging and selected topics in Power Electronics*, *4*(1), pp.116-125. https://doi.org/10.1109/JESTPE.2015.2490549

[32] Wang, X. and Blaabjerg, F., 2019. Harmonic stability in power electronic-based power systems: Concept, modeling, and analysis. *IEEE Transactions on Smart Grid*, *10*(3), pp.2858-2870. https://doi.org/10.1109/TSG.2018.2812712

[33] Ruan, X., Wang, X., Pan, D., Yang, D., Li, W. and Bao, C., 2018. *Control techniques for LCL-type grid-connected inverters*. Springer Singapore. https://doi.org/10.1007/978-981-10-4277-5

[34] He, Y., Wang, X., Ruan, X., Pan, D., Xu, X. and Liu, F., 2019. Capacitor-current proportional-integral positive feedback active damping for LCL-type grid-connected inverter to achieve high robustness against grid impedance variation. *IEEE Transactions on Power Electronics*, *34*(12), pp.12423-12436. https://doi.org/10.1109/TPEL.2019.2906217

[35] Lu, M., Al-Durra, A., Muyeen, S.M., Leng, S., Loh, P.C. and Blaabjerg, F., 2018. Benchmarking of stability and robustness against grid impedance variation for LCL-filtered grid-interfacing inverters. *IEEE Transactions on Power Electronics*, *33*(10), pp.9033-9046. https://doi.org/10.1109/TPEL.2017.2784685

[36] Harnefors, L., Yepes, A.G., Vidal, A. and Doval-Gandoy, J., 2014. Passivity-based stabilization of resonant current controllers with consideration of time delay. *IEEE Transactions on Power Electronics*, *29*(12), pp.6260-6263. https://doi.org/10.1109/TPEL.2014.2328669

[37] Faiz, M.T., Khan, M.M., Jianming, X., Ali, M., Habib, S., Hashmi, K. and Tang, H., 2020. Capacitor voltage damping based on parallel feedforward compensation method for LCL-filter grid-connected inverter. *IEEE Transactions on Industry Applications*, *56*(1), pp.837-849. https://doi.org/10.1109/TIA.2019.2951115

[38] Bimarta, R. and Kim, K.H., 2020. A robust frequency-adaptive current control of a grid-connected inverter based on LMI-LQR under polytopic uncertainties. *IEEE Access*, *8*, pp.28756-

28773.
https://doi.org/10.1109/ACCESS.2020.2972028
[39] Padmanaban, S., Priyadarshi, N., Bhaskar, M.S., Holm-Nielsen, J.B., Hossain, E. and Azam, F., 2019. A hybrid photovoltaic-fuel cell for grid integration with jaya-based maximum power point tracking: experimental performance evaluation. *IEEE Access*, *7*, pp.82978-82990. https://doi.org/10.1109/ACCESS.2019.2924264
[40] Kim, Y.J. and Kim, H., 2019. Optimal design of LCL filter in grid- connected inverters. *IET Power Electronics*, *12*(7), pp.1774-1782. https://doi.org/10.1049/iet-pel.2018.5518
[41] Dragičević, T., Zheng, C., Rodriguez, J. and Blaabjerg, F., 2020. Robust quasi-predictive control of LCL-filtered grid converters. *IEEE Transactions on Power Electronics*, 35(2), pp.1934-1946. https://doi.org/10.1109/TPEL.2019.2916604
[42] Hosseinpour, M. and Kholousi, A., 2023. Design and Analysis of LCL-type Grid-Connected PV Power Conditioning System Based on Positive Virtual Impedance Capacitor-Current Feedback Active Damping. *Journal of Solar Energy Research*, *8*(2), pp.1497-1515. https://doi.org/10.22059/jser.2023.357089.1286